Polariton drag enabled quantum geometric photocurrents in high-symmetry materials

Ying Xiong,[1] Li-kun Shi,[2] and Justin C. W. Song[1,*]
[1]*Division of Physics and Applied Physics, Nanyang Technological University, 637371 Singapore*
[2]*Max Planck Institute for the Physics of Complex Systems, Dresden 01187, Germany*

(Received 15 October 2021; revised 19 October 2022; accepted 20 October 2022; published 29 November 2022)

Lowered symmetry enables access to a wide set of responses not typically accessible in high symmetry materials. Prime examples are time-reversal forbidden quantum geometric photocurrent responses (e.g., linear injection and circular shift photocurrents) that are thought to vanish in nonmagnetic materials. Here we argue that polariton drag processes enable to unblock such quantum geometric photocurrents even in nonmagnetic and centrosymmetric materials. Strikingly, we uncover how a cooperative effect between finite **q** irradiation and the Fermi surface position leads to a polariton selective photoexcitation (PSP). PSP enables to directly address carriers within tight momentum resolved windows of the Fermi surface to yield giant enhancements of quantum geometric photocurrents. This selectivity enables to directly track momentum resolved quantum geometric quantities along the Fermi surface providing a new tool to interrogate the quantum geometry of high symmetry materials.

DOI: 10.1103/PhysRevB.106.205423

Quantum geometry can play an essential role in light-matter interaction. A prime example are bulk rectified currents such as the injection and shift photocurrents: these have strength determined by quantum geometric quantities (e.g., Berry curvature), and as such, are now actively used as sensitive probes of the structure of Bloch wave functions in quantum materials [1–8]. Access to such photocurrents, however, requires lowered symmetry. For instance, circular shift (CS) and linear injection (LI) photocurrents are odd under time-reversal, $\mathcal{T}$, as well as inversion, $\mathcal{P}$. They are thought to only manifest in parity violating magnetic materials [3,8–10] such as antiferromagnets. Consequently, the quantum geometric quantities associated with LI/CS photocurrents (e.g., quantum metric/circular shift vector) are typically inaccessible to photocurrent probes in high symmetry materials.

Here we consider a different strategy to achieve lowered symmetry: by employing the spatial structure of electromagnetic (EM) fields (e.g., in nanophotonics [11–13] or under oblique incident irradiation). A case in point is the *drag* induced by photons or polaritons (e.g., propagating plasmon with a finite **q**). In the polariton/photon-drag (PD) processes, the finite **q** momentum structure of traveling EM fields can induce nonvertical interband transitions. Indeed, exploiting PD has a long history: e.g., photon drag via direct optical transfer [14–21] or indirect processes [20–22] can be used to drive photocurrents, nanophotonic confinement can enable access to multipolar transitions [23].

Here we argue that PD strategies can also be used to induce nonvertical interband transitions and bulk CS and LI photocurrents even in nonmagnetic and inversion symmetric materials. Interestingly, PD strategies do not activate all charge quantum geometric photocurrents: we find PD linear shift and circular injection photocurrents still vanish in centrosymmetric and nonmagnetic materials. This delineation highlights the central role quantum geometry plays in PD photocurrents: PD photocurrents depend on both quantum geometry and drag-induced velocity.

Surprisingly, we find that PD can enable polariton selective photoexcitation (PSP) of carriers: i.e., by tuning both the polariton energy and its wavevector, only carriers within a selective window of momentum and energy are photoexcited. As we explain below, PSP produces a rich phenomenology including resonant enhancements and Fermi surface dependent photocurrents that arise from interband transitions (see Figs. 1 and 2). Importantly, when the momentum selective window of PSP is tightened, it can enable a photocurrent probe of momentum resolved quantum geometric quantities.

A striking platform to realize strong PD photocurrents are hybrid plasmonic heterostructures [11–13,24], where a quantum material is placed on top of a plasmonic material [Fig. 2(a)]. In these, oblique incident light excites the plasmons in the plasmonic material, and the propagating EM field of the plasmon in turn induces a PD current in the quantum material. The wavevector of the plasmonic field can be tuned by dielectric constant of the substrate [24] or by nanophotonic engineering [12,13]. Hybrid plasmonic heterostructures enable to achieve large **q**-wavevectors far larger than that of free space, and as we explain below, enhance PD photocurrents.

As a concrete illustration, we show a PSP protocol for quantum geometric PD photocurrents in bilayer graphene (BLG)–a centrosymmetric and nonmagnetic material. We find PSP in BLG can induce large nonlinear susceptibilities with magnitudes comparable to that of ferroelectric materials [25] (where inversion symmetry is broken) for values of **q** that can be readily achievable in hybrid plasmonic heterostructures. Strikingly, we find PD LI photocurrents tracks the

*Corresponding author: justinsong@ntu.edu.sg

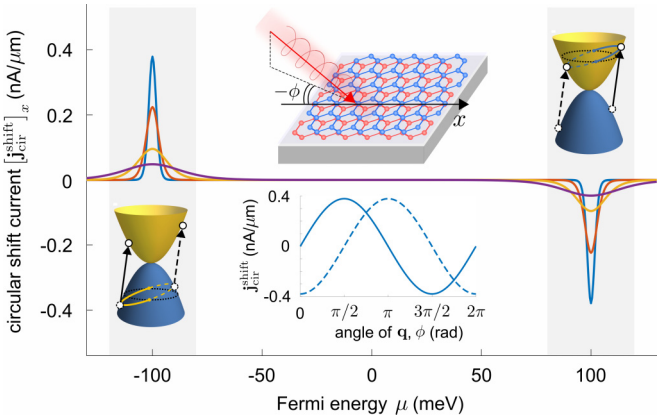

FIG. 1. PD charge circular shift photocurrent in BLG displaying resonant like features close to $\mu = \pm\hbar\omega/2$; these arise from (inset) polariton selective photoexcitation (PSP) wherein carries within a momentum window are excited, see also Figs. 2 and 3. Blue, orange, yellow and purple curves are obtained at temperatures 10 K, 20 K, 50 K, and 100 K. Parameters used: $\hbar\omega = 200$ meV, $|\mathbf{q}| = 0.001\text{nm}^{-1}$ corresponding that to free space photons, $|\mathbf{E}| = 0.05$ V/μm, and $\phi = \pi/2$. (inset, middle upper panel) Schematic diagram of BLG irradiated by an oblique incidence of light. (inset, middle lower panel) Circular shift current as a function of ϕ for $\mu = -100$ meV. The solid (dashed) lines indicate $[\mathbf{j}_{\rm cir}^{\rm shfit}]_x$ ($[\mathbf{j}_{\rm cir}^{\rm shfit}]_y$).

momentum-resolved quantum metric dipole along the Fermi surface (see Fig. 3). This demonstrates the power of polariton drag processes in unblocking and amplifying quantum geometric photocurrents.

I. PD INJECTION AND SHIFT PHOTOCURRENTS

We begin by considering a material irradiated by incident finite $\mathbf{q}$ EM fields with electric field profile $\boldsymbol{\mathcal{E}}(\mathbf{r}, t) = (1/2)\sum_{\pm} \mathbf{E}_{\pm} e^{\pm i\mathbf{q}\cdot\mathbf{r}\mp i\omega t}$ with $\mathbf{E}_{\pm}$ the complex electric field amplitude where $\mathbf{E}_{+} = (\mathbf{E}_{-})^{*} = \mathbf{E}$. The oscillating EM fields induce real interband electronic transitions. As a concrete demonstration and for clarity and brevity of presentation, we focus on a two-band system where EM radiation induces transitions between the conduction c and the valence v bands. Considering momentum and energy conservation, EM radiation induces nonvertical transitions between pairs of Bloch states $|u_v(\mathbf{k}_{-})\rangle$ and $|u_c(\mathbf{k}_{+})\rangle$, where $\mathbf{k}_{-} = \mathbf{k} - \mathbf{q}/2$ and $\mathbf{k}_{+} = \mathbf{k} + \mathbf{q}/2$. The transition rates can be readily calculated by Fermi's golden rule: $W^{\pm}_{i\to f} = (2\pi/\hbar)|V^{\pm}_{i\to f}|^2 f_i(1 - f_f)\delta(\epsilon_f - \epsilon_i \mp \hbar\omega)$, where $V^{\pm}_{i\to f} = e/(2\omega)\langle f|\mathbf{E}^{\pm}\cdot\hat{\mathbf{v}}|i\rangle$ is the interband transition matrix element, $\hat{\mathbf{v}}$ is the velocity operator, and $f_{i(f)}$ and $\epsilon_{i(f)}$ are the electron distribution function and energy for the initial (final) states respectively. Accounting for the changes to electron position and velocity upon interband transition directly produce (interband) quantum geometric photocurrents [8]. In the following, we focus on the PD photocurrents induced by interband transitions. These are expected to dominate in the high frequency regime when the polariton frequency ω is much larger than the carrier scattering rate [26].

To see this, we first examine the shift current that arises from the real space displacement of electrons (charge $e < 0$)

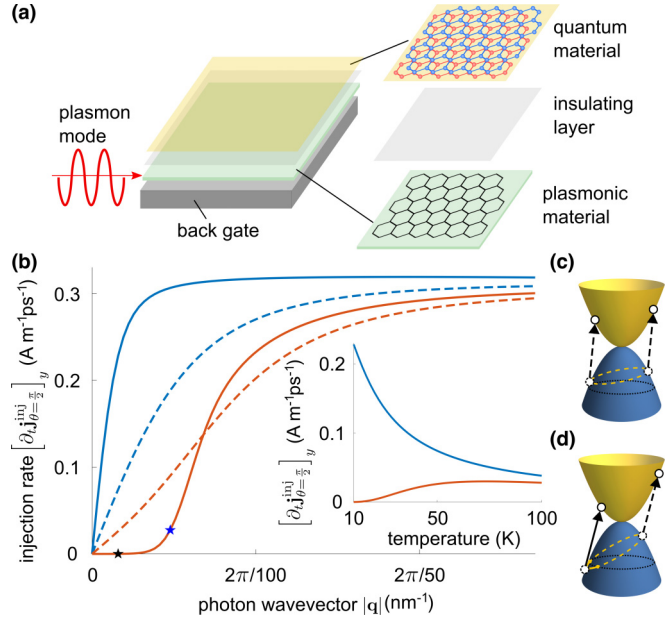

FIG. 2. PD charge LI photocurrent in BLG. (a) Schematic diagram of a hybrid quantum material/host plasmonic material system, in which the electromagnetic field of the plasmons in the proximal host material (green) induces nonvertical interband transitions and PD photocurrents in the quantum material (yellow). (b) $|\mathbf{q}|$ dependence of PD LI photocurrent for Fermi energies $\mu = -100$ meV (blue) and $\mu = -110$ meV (orange). The solid and dashed lines denote temperatures of 10 K and 50 K. The black and blue stars correspond to $|\mathbf{q}| = 0.01$ nm^{-1} (smaller than q_c) and $|\mathbf{q}| = 0.03$ nm^{-1} (i.e., $|\mathbf{q}| \gtrsim q_c$). (inset) Temperature dependence of the PD LI photocurrent at $|\mathbf{q}| = 0.01$ nm^{-1} for different Fermi energies (color code is the same as in main panel). We have set $|\mathbf{E}| = 0.05\text{V}/\mu\text{m}$ and $\phi = \pi/2$. (c, d) Schematic illustration of the transition contours (yellow) for $|\mathbf{q}| < q_c$ (c) and $|\mathbf{q}| \sim q_c$ (d). The yellow solid (dashed) lines indicate the occupied (unoccupied) section of the transition contour. The black dotted line indicates the Fermi surface. The injection photocurrent can be estimated from the injection rate by accounting for the relaxation or accumulation time, see description in text.

that undergo interband transitions [8,27,28]. Accounting for the transition rate, the finite $\mathbf{q}$ shift current is [29]

$$\mathbf{j}^{\rm shift}(\mathbf{q}) = C\sum_{\mathbf{k}} \rho(\mathbf{k}, \mathbf{q})|\mathbf{E}\cdot\boldsymbol{\nu}_{cv}(\mathbf{k}, \mathbf{q})|^2\mathbf{R}(\mathbf{k}, \mathbf{q}), \qquad (1)$$

where $C = -e^3\pi/(2\hbar\omega^2)$, the occupation factor is $\rho(\mathbf{k}, \mathbf{q}) = f_{cv}(\mathbf{k}, \mathbf{q})\delta(\epsilon_{cv}(\mathbf{k}, \mathbf{q}) - \hbar\omega)$, the Fermi function difference is $f_{cv}(\mathbf{k}, \mathbf{q}) = f(\epsilon_c(\mathbf{k}_{+})) - f(\epsilon_v(\mathbf{k}_{-}))$ with the interband transition energy $\epsilon_{cv}(\mathbf{k}, \mathbf{q}) = \epsilon_c(\mathbf{k}_{+}) - \epsilon_v(\mathbf{k}_{-})$, the velocity matrix element is $\boldsymbol{\nu}_{cv}(\mathbf{k}, \mathbf{q}) = \langle u_c(\mathbf{k}_{+})|\hat{\mathbf{v}}(\mathbf{k})|u_v(\mathbf{k}_{-})\rangle$, and $\mathbf{R}(\mathbf{k}, \mathbf{q})$ is the real-space displacement [1,8,30], also called the shift vector, when a valence electron transits to the conduction band. It is directly related to a Pancharatnam-Berry (geometric) phase $\mathbf{R}(\mathbf{k}, \mathbf{q}) = \lim_{\delta\mathbf{k}\to 0}\nabla_{\delta\mathbf{k}}\arg\mathcal{W}(\mathbf{k}, \delta\mathbf{k}, \mathbf{q})$ accrued during the transition (see Supplemental Material, SM [31]):

$$\mathcal{W}(\mathbf{k}, \delta\mathbf{k}, \mathbf{q}) = \langle u_v(\mathbf{k}_{-})|u_v(\mathbf{k}'_{-})\rangle[\hat{\mathbf{e}}\cdot\langle u_v(\mathbf{k}'_{-})|\hat{\mathbf{v}}|u_c(\mathbf{k}'_{+})\rangle] \cdot\langle u_c(\mathbf{k}'_{+})|u_c(\mathbf{k}_{+})\rangle\langle u_c(\mathbf{k}_{+})|u_v(\mathbf{k}_{-})\rangle, \qquad (2)$$

TABLE I. Symmetry relations for PD charge shift and injection photocurrents. Photocurrents for linear polarized irradiation are denoted θ whereas helicity dependent photocurrents are denoted "cir". We find that PD $\mathbf{q} \neq 0$ LI and CS charge photocurrents are allowed in both $\mathcal{T}$- and $\mathcal{P}$-preserving materials (indicated by ticks, third row). In contrast, when $\mathbf{q} = 0$ LI and CS photocurrents vanish in $\mathcal{T}$-preserving but $\mathcal{P}$-breaking materials.

charge photocurrent	linear injection	circular injection	linear shift	circular shift
$\mathcal{P}$-symmetry	$\partial_t \mathbf{j}_\theta(\mathbf{q}) = -\partial_t \mathbf{j}_\theta(-\mathbf{q})$	$\partial_t \mathbf{j}_{\rm cir}(\mathbf{q}) = -\partial_t \mathbf{j}_{\rm cir}(-\mathbf{q})$	$\mathbf{j}_\theta(\mathbf{q}) = -\mathbf{j}_\theta(-\mathbf{q})$	$\mathbf{j}_{\rm cir}(\mathbf{q}) = -\mathbf{j}_{\rm cir}(-\mathbf{q})$
$\mathcal{T}$-symmetry	$\partial_t \mathbf{j}_\theta(\mathbf{q}) = -\partial_t \mathbf{j}_\theta(-\mathbf{q})$	$\partial_t \mathbf{j}_{\rm cir}(\mathbf{q}) = \partial_t \mathbf{j}_{\rm cir}(-\mathbf{q})$	$\mathbf{j}_\theta(\mathbf{q}) = \mathbf{j}_\theta(-\mathbf{q})$	$\mathbf{j}_{\rm cir}(\mathbf{q}) = -\mathbf{j}_{\rm cir}(-\mathbf{q})$
$\mathbf{q} \neq 0$ ($\mathcal{T}$ & $\mathcal{P}$ symmetry)	✓	✗	✗	✓
$\mathbf{q} = 0$ ($\mathcal{T}$ symmetry only)	✗	✓	✓	✗

where $\hat{\mathbf{e}}$ is the polarization, $\mathbf{k}'_- = \mathbf{k}_- + \delta\mathbf{k}$, and $\mathbf{k}'_+ = \mathbf{k}_+ + \delta\mathbf{k}$.

In the same fashion, the injection current rate arises from a change of velocity when a carrier undergoes interband transitions [8] and can be written as

$$\partial_t \mathbf{j}^{\rm inj}(\mathbf{q}) = C \sum_{\mathbf{k}} \rho(\mathbf{k}, \mathbf{q}) |\mathbf{E} \cdot \boldsymbol{v}_{cv}(\mathbf{k}, \mathbf{q})|^2 \boldsymbol{\Delta}(\mathbf{k}, \mathbf{q}), \quad (3)$$

where $\boldsymbol{\Delta}(\mathbf{k}, \mathbf{q}) = \mathbf{v}_c(\mathbf{k}_+) - \mathbf{v}_v(\mathbf{k}_-)$ is the change in carrier velocity. In the same fashion as above, the transition matrix elements are closely related to an interband quantum geometric tensor. As we will see below, this fact, together with PSP, will enable to probe the momentum resolved quantum geometry of Bloch bands.

We note that Eq. (3) describes a rate of change of injection current. In physical situations, this accumulation of current is often cut by a finite relaxation time or in the case of ultrashort pulses of EM radiation where the pulsewidth duration is shorter than relaxation time, by the pulsewidth. As such, the injection current can be estimated as $\mathbf{j}^{\rm inj}(\mathbf{q}) = \tau \partial_t \mathbf{j}^{\rm inj}(\mathbf{q})$ [2,32–34], where τ is an effective time over which the injection photocurrent relaxes/accumulates. In steady-state measurements, τ is often approximated by the momentum relaxation time of the photoexcited hot-carriers [2,32]; we note, parenthetically, that understanding the precise interplay between relaxation and quantum geometric photocurrents is a subject of current intense research [33,35]. The relaxation time can even be band and $\mathbf{k}$ dependent [14,19,20]. In what follows, to highlight the PSP effect, we will focus on the ultrafast photocurrent regime.

II. UNBLOCKING TIME-REVERSAL FORBIDDEN PHOTOCURRENTS

As we now argue, both $\mathbf{j}^{\rm shift}(\mathbf{q})$ and $\mathbf{j}^{\rm inj}(\mathbf{q})$ in Eq. (1) and Eq. (3) possess markedly different symmetry properties as compared to their vertical transition counterparts. We perform a symmetry analysis to obtain the PD photocurrent symmetry properties shown in Table I, see SM for details. In populating the table, we have denoted photocurrents $\mathbf{j}_\theta$ arising from linearly polarized light $\mathbf{E} = \mathbf{E}^\theta = E(\hat{\mathbf{x}}\cos\theta + \hat{\mathbf{y}}\sin\theta)$ with the subscript index θ. In analyzing the circularly polarized irradiation, we have focused on the photocurrent $\mathbf{j}_{\rm cir}$ that depends on light helicity η [with electric field $\mathbf{E}^\eta = E(\hat{\mathbf{x}} + i\eta\hat{\mathbf{y}})$].

Of particular note are the LI and CS photocurrents. While forbidden when $\mathbf{q} = 0$ in $\mathcal{T}$ invariant nonmagnetic materials, nonvertical transitions (PD activated) when $\mathbf{q} \neq 0$ enable to generate finite PD LI and CS photocurrents even in materials with both $\mathcal{T}$ and $\mathcal{P}$ symmetries (third row). This is because LI/CS photocurrents display an odd parity as $\mathbf{q} \to -\mathbf{q}$ for either $\mathcal{T}$ and $\mathcal{P}$ symmetries: $\mathbf{q}$ controls the direction of the PD LI/CS photocurrent generated.

Interestingly, finite $\mathbf{q}$ circular injection and linear shift charge photocurrents *vanish* in materials possessing both $\mathcal{T}$ and $\mathcal{P}$ symmetries: not all photocurrents are enabled by finite $\mathbf{q}$; this mirrors a similar vanishing in $\mathcal{PT}$ symmetric parity-violating magnets at $\mathbf{q} = 0$ [3,8]. We note that while here we have concentrated on charge photocurrent response, PD *spin* photocurrents are expected to have different transformation properties from that of Table I [29]. Lastly, we note that while we have focused on interband photocurrents, finite $\mathbf{q}$ may also unblock intraband photocurrents that can depend on extrinsic scattering processes in nonmagnetic and centrosymmetric metals [26].

III. PD CS AND LI PHOTOCURRENTS IN BLG

As a concrete demonstration of how nonvertical transitions unblock quantum geometric photocurrents, we examine CS and LI photocurrents in gapless BLG. Notably, BLG is a centrosymmetric semimetal that preserves $\mathcal{T}$-symmetry; its low energy Hamiltonian can be written as $H(\mathbf{p}) = H_0(\mathbf{p}) + H_w(\mathbf{p})$ [36], where

$$H_0(\mathbf{p}) = -\frac{\hbar^2}{2m}\left[(p_x^2 - p_y^2)\sigma_x + 2\zeta p_x p_y \sigma_y\right],$$
$$H_w(\mathbf{p}) = \hbar v_3(\zeta p_x \sigma_x - p_y \sigma_y). \quad (4)$$

Here $\mathbf{p} = \mathbf{k} - \mathbf{K}_\zeta$ is the Bloch wavevector measured from K_ζ points, $\zeta = \pm$ is the valley index, and m is the effective mass. $H_w(\mathbf{p})$ describes trigonal warping, consistent with BLG's threefold rotational symmetry C_3^z. Additionally, BLG also possesses mirror axes (e.g., y-axis act as a mirror plane).

We first examine the PD CS photocurrent. We evaluate Eq. (1) for a circularly polarized beam ($\hbar\omega = 200$ meV) with in-plane photon wavevector $\mathbf{q} \parallel \hat{\mathbf{y}}$ along a mirror axis in BLG. This yields a sizable PD $\mathbf{j}_{\rm cir}^{\rm shift}$ in Fig. 1. We note that point group symmetries can greatly constrain the direction of the PD photocurrents for a given polarization. To see this, consider mirror symmetry $\mathcal{M}_y : (x, y) \to (-x, y)$ with the polariton wavevector $\mathbf{q}$ along the mirror axis. For circularly polarized light, we find that the momentum resolved transition rate obeys $|\mathbf{E}^\eta \cdot \mathbf{v}_{cv}(\mathbf{k}, \mathbf{q})|^2 = |\mathbf{E}^{-\eta} \cdot \mathbf{v}_{cv}(\mathcal{M}_y\mathbf{k}, \mathbf{q})|^2$,

while the shift vector satisfies (see SM for detailed analysis)

$$R_x^{\eta}(\mathbf{k},\mathbf{q}) = -R_x^{-\eta}(\mathcal{M}_y\mathbf{k},\mathbf{q}), \quad R_y^{\eta}(\mathbf{k},\mathbf{q}) = R_y^{-\eta}(\mathcal{M}_y\mathbf{k},\mathbf{q}). \tag{5}$$

As a result, when $\mathbf{q}$ is directed parallel to mirror plane, we find the PD circular shift photocurrent $\mathbf{j}_{\rm cir}^{\rm shift}$ is transverse. This is verified in the numerical simulation for BLG, as shown in Fig. 1(inset).

Strikingly, PD CS photocurrents display large peaks centered at $\mu = \pm\hbar\omega/2$ (Fig. 1). These resonant peaks arise from PSP: when the (tilted) interband transition energy contours [defined by $\delta(\epsilon_{cv}^{\zeta}(\mathbf{p},\mathbf{q}) - \hbar\omega)$] intersect with the Fermi surface. In this, the combined action of the finite $\hbar\mathbf{q}$ momentum transfer as well as the position of the Fermi surface ensures that only carriers in parts of the interband transition energy contours $\delta(\epsilon_{cv}^{\zeta}(\mathbf{p},\mathbf{q}) - \hbar\omega)$ are excited [as captured by the joint occupation factor $\rho(\mathbf{p},\mathbf{q})$ in Eq. (1)]. PSP induces a large asymmetry in sampling the circular shift vector (see SM) to produce a giant enhancement of CS photocurrent.

Interestingly, the part of the interband transition energy contour that is excited depends directly on μ: when μ is tuned from $-\hbar\omega/2 \to \hbar\omega/2$ the allowed excitations flip (see inset of Fig. 1 and SM) thereby sampling a different window of circular shift vector $\mathbf{R}^{\eta,\zeta}(\mathbf{p},\mathbf{q})$, where η denotes the shift vector induced by light with helicity η. Indeed, this sampling is angle sensitive: by rotating azimuthal angle ϕ, CS photocurrent similarly rotates [Fig. 1(inset)] displaying a photocurrent that is locked to the symmetry breaking axis determined by $\mathbf{q}$. When μ is tuned away from $\pm\hbar\omega/2$, PD $\mathbf{j}_{\rm cir}^{\rm shift}$ falls steeply [Fig. 1(a)]; in this regime $\mathbf{j}_{\rm cir}^{\rm shift}$ vanishes due to the presence of c, v band symmetry in Eq. (4), see SM. We note that such c, v band symmetry is strongly broken by tuning the Fermi surface so that it intersects with the interband transition contour, leading to PSP and large photoresponse.

PSP-induced peak features are ubiquitous for PD photocurrents and also extend to PD LI photocurrents. Indeed, similar peaks close to $\mu = \pm\hbar\omega/2$ have been predicted for oblique incident far-field linearly polarized light at low temperature in graphene [16]. We note, in a similar fashion described above for PD CS photocurrents, the direction of PD LI photocurrent also exhibits a strong dependence of high-symmetry axes in the material; in particular, it is highly sensitive to how light polarization is aligned with the mirror axes (see SM for details). To see this, consider the case when $\mathbf{q}$ is along the mirror axis, so that

$$\Delta_x(\mathbf{k},\mathbf{q}) = -\Delta_x(\mathcal{M}_y\mathbf{k},\mathbf{q}), \quad \Delta_y(\mathbf{k},\mathbf{q}) = \Delta_y(\mathcal{M}_y\mathbf{k},\mathbf{q}). \tag{6}$$

For the special case of light polarized either parallel or perpendicular to the mirror axis, we have $|\mathbf{E}^{\theta}\cdot\mathbf{v}_{cv}(\mathbf{k},\mathbf{q})|^2 = |\mathbf{E}^{\theta}\cdot\mathbf{v}_{cv}(\mathcal{M}_y\mathbf{k},\mathbf{q})|^2$, yielding PD LI photocurrent flowing along $\mathbf{q}$. For light polarized away from these directions, mirror symmetry is broken and PD LI photocurrents need not flow purely along $\mathbf{q}$, see SM.

In the following, we concentrate on a different regime for PD LI photocurrents: μ is detuned away from $\pm\hbar\omega/2$. In this detuned situation [red curve Fig. 2(b)], small values of $|\mathbf{q}| \ll q_c$ do not produce an LI photocurrent since the transition contour does not intersect the Fermi surface [Fig. 2(c)]; here q_c is a threshold wavevector at which the transition contour [defined by $\epsilon_{cv}(\mathbf{k},\mathbf{q}) = \hbar\omega$] just intersects the Fermi surface [Fig. 2(d)]. In the conduction/valence band, the transition contour is given by $\epsilon_{c,v}(\mathbf{k} \pm \mathbf{q}/2)$. For small detuning, q_c can be estimated as $q_c \approx 2||\mu| - \hbar\omega/2|/\hbar\tilde{v}$ where $\tilde{v} = \max[\tilde{\mathbf{v}}_{c,v}\cdot\hat{\mathbf{q}}]$, and $\tilde{\mathbf{v}}_{c,v} = (1/\hbar)[\nabla_{\mathbf{k}}\epsilon_{c,v}(\mathbf{k})|_{\epsilon_{c,v}=\pm\hbar\omega/2}]$. When $|\mathbf{q}| \gtrsim q_c$, LI photocurrent rapidly turns on: this arises from a tight PSP window of photoexcited carriers. As illustrated in Fig. 2(b), for a detuning of $||\mu| - \hbar\omega/2| = 10$ meV, the LI photocurrent turns on at $q_c \approx 0.03\ \mathrm{nm}^{-1}$ (blue star), which is about 30 times larger than that of free space light and can be readily achieved in graphene based plasmonic materials [24].

This behavior contrasts with that of $\mu = -\hbar\omega/2$ case (blue curve) where PD LI photocurrents flow even for arbitrarily small but finite values of $\mathbf{q}$ since $q_c = 0$: even small $\mathbf{q}$ produce a wide window (in momentum space) of PSP carriers. This difference in PSP windows for $|\mu| = \hbar\omega/2$ vs $\mu \neq \hbar\omega/2$ leads to contrasting temperature dependence. When $|\mu| = \hbar\omega/2$ PD LI photocurrents increase as temperature decreases. In contrast, when $\mu \neq \hbar\omega/2$, PD LI photocurrents display a complex $\mathbf{q}$-dependent temperature dependence since $\mathbf{q}$ controls the regions of the interband transition contour that dip below the Fermi surface. When $\mathbf{q}$ is further increased beyond q_c, the LI photocurrent saturates and become relative insensitive to temperature, see Fig. 2(b) [solid vs dashed]. Note that in Fig. 2(b), we have plotted the LI photocurrent for a range of wavevectors up to $|\mathbf{q}| = 0.17\ \mathrm{nm}^{-1}$, which corresponds to a plasmonic field confinement of 170 times and can be achieved via nanophotonic engineering [12,13].

Strikingly, when μ is detuned away from $|\mu| = \hbar\omega/2$ and by selecting $|\mathbf{q}| \approx q_c$ just at threshold, a highly momentum selective PSP window can be engineered [Figs. 3(a)–3(d) where the amplitude of $\rho(\mathbf{p},\mathbf{q})$ is plotted]. At these $|\mathbf{q}|$ values, the transition contour just intersects the Fermi surface. As a result, PSP enables angle-selective (controlled by the direction of the polariton wavevector, ϕ) excitation of carriers close to the Fermi surface (dashed black line); this mirrors means of momentum resolution found in angle-resolved photoemission. We note that when μ is tuned from the valence band to the conduction band, charge carriers from the opposite side of the Fermi surface are sampled.

Here we have chosen a Fermi energy detuning of 10 meV away from $-\hbar\omega/2$ and the plasmon polariton wavevector $|\mathbf{q}| = 0.03\ \mathrm{nm}^{-1}$. In this regime, k_BT (employed in Fig. 3) is much smaller than the detuning, allowing for a good momentum resolution of PSP. We note that in principle, such selective photoexcitation can also be achieved using wavevectors that are smaller (e.g., using free space photons). However, the corresponding detuning to achieve tight momentum resolution will be similarly smaller, making such selectivity highly sensitive to thermal broadening and easily smeared.

The tight window of PSP-induced excitation enables to probe momentum resolved quantum geometry near the Fermi surface. To see this, consider the PD *linear* injection current in Eq. (3) written out in component form as $\partial_t \mathbf{j}_{\theta}^{\rm inj}(\mathbf{q}) = -e^3\pi/(2\hbar)\sum_{\mathbf{k},a,b}\rho(\mathbf{k},\mathbf{q})\mathbf{\Delta}(\mathbf{k},\mathbf{q})G_{ba}^{cv}(\mathbf{k},\mathbf{q})E_bE_a^*$, where

$$G_{ba}^{cv}(\mathbf{k},\mathbf{q}) = \mathrm{Re}\left\{r_{cv}^{b}(\mathbf{k},\mathbf{q})\left[r_{cv}^{a}(\mathbf{k},\mathbf{q})\right]^*\right\} \tag{7}$$

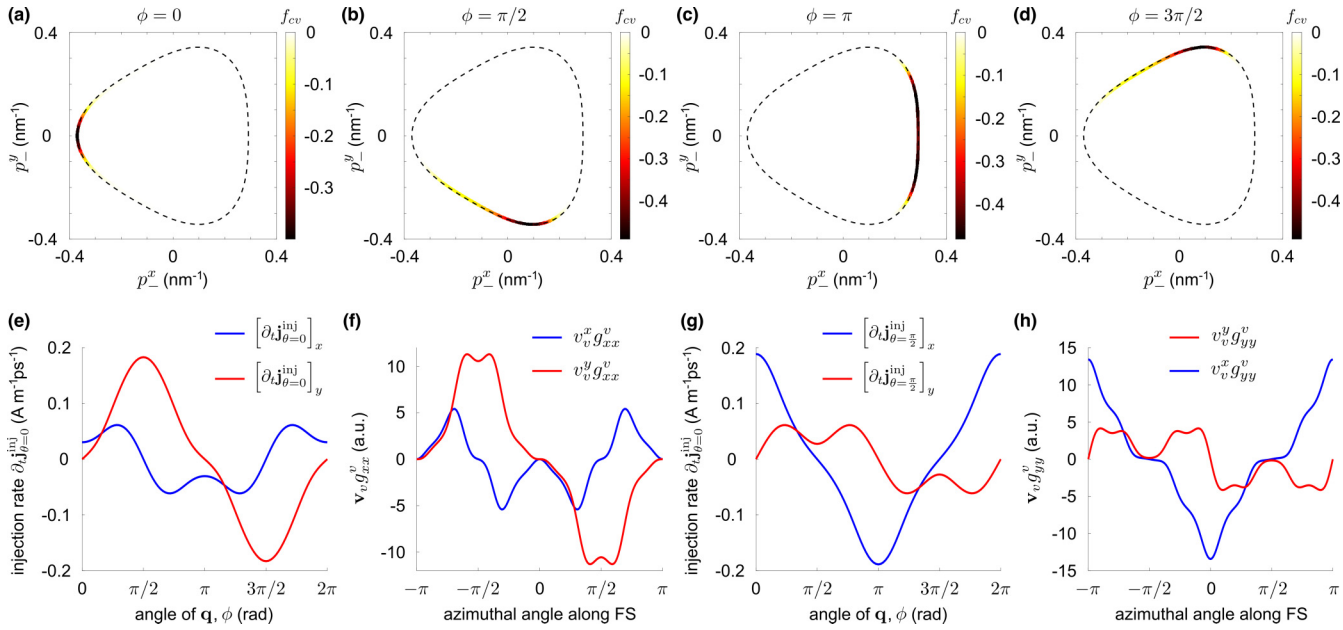

FIG. 3. PD photocurrent as a momentum resolved tool to probe quantum geometry. (a-d) Partial excitation of charge carriers near the Fermi surface in k-space (coloured segment). Here $\mathbf{p}_- = \mathbf{p} - \mathbf{q}/2$. (e,g) LI photocurrents as a function of ϕ at a fixed magnitude $|\mathbf{q}| = 0.03$ nm^{-1} and $\mu = -110$ meV for x-polarized (e) and y-polarized (g) light in BLG. Here we have used $T = 10$ K and $|\mathbf{E}| = 0.05$ V/μm. The photocurrents enable to track the corresponding quantum metric dipoles shown in (f) and (h) along the Fermi surface (FS); here we have summed over both K and K' valleys in Eq. (4). We note that for $\phi = 0$, the charge carriers close to azimuthal angle $-\pi$ along the FS are sampled.

is a generalised $\mathbf{q}$-dependent c, v band resolved interband quantum metric (see SM) with $r^a_{cv}(\mathbf{k}, \mathbf{q}) = \hbar v^a_{cv}(\mathbf{k}, \mathbf{q})/i[\epsilon_c(\mathbf{k}_+) - \epsilon_v(\mathbf{k}_-)]$. Interestingly, in the two-band limit that we concentrate on [Eq. (4)] and when polariton wavevector is relatively small, $|\mathbf{q}| \ll |\mathbf{k}|$, $\mathbf{\Delta}(\mathbf{k}, \mathbf{q}) G^{cv}_{ba}(\mathbf{k}, \mathbf{q})$ approximates the direct quantum metric dipole $\mathbf{\Delta}(\mathbf{k}, 0)\text{Re}\,[r^b_{cv}(\mathbf{k}, 0) r^a_{vc}(\mathbf{k}, 0)] = -2\mathbf{v}_v(\mathbf{k}) g^v_{ba}(\mathbf{k})$ [8], where in the last equality we specialized to BLG in Eq. (4) and $g^v_{ba}(\mathbf{k}) dk_a dk_b = 1 - |\langle u_v(\mathbf{k}) | u_v(\mathbf{k} + d\mathbf{k})\rangle|^2$ is the valence band quantum metric. For comparison with the numerical photocurrent simulation in Fig. 3, here we explicitly write down $g^v_{xx}(\mathbf{p})$ and $g^v_{yy}(\mathbf{p})$ at each valley:

$$g^v_{xx}(\mathbf{p}) = \frac{\left[\left(-\frac{\hbar^2}{m} p_x + \hbar v_3 \zeta\right) \sin\varphi_{\zeta,\mathbf{p}} + \frac{\hbar^2}{m} \zeta p_y \cos\varphi_{\zeta,\mathbf{q}}\right]^2}{4[d(\mathbf{p})]^2},$$
$$g^v_{yy}(\mathbf{p}) = \frac{\left[\frac{\hbar^2}{m} p_y \sin\varphi_{\zeta,\mathbf{p}} + \left(\frac{\hbar^2}{m} \zeta p_x + \hbar v_3\right) \cos\varphi_{\zeta,\mathbf{p}}\right]^2}{4[d(\mathbf{p})]^2}, \quad (8)$$

where $d(\mathbf{p}) = \sqrt{d_1^2 + d_2^2}$ is the conduction band energy, $d_1 = -\frac{\hbar^2}{2m}(p_x^2 - p_y^2) + \hbar v_3 \zeta p_x$, $d_2 = -\frac{\hbar^2}{m} \zeta p_x p_y - \hbar v_3 p_y$, and $\tan^{-1} \varphi_{\zeta,\mathbf{p}} = d_2/d_1$. As we discuss below, the corresponding momentum resolved quantum metric dipoles Figs. 3(f) and 3(h) provide a good estimate for the PD LI photocurrents for the two-band Hamiltonian in Eq. (4). Of course, in a more general multiband Hamiltonian, PD LI photocurrents track the generalized interband quantum metric, see Eq. (7).

Given the tight momentum selective window accessed in Figs. 3(a)–3(d), by fixing the magnitude of $\mathbf{q}$ while varying its direction, the LI photocurrents enables to track the quantum metric dipole $g^v_{ba}(\mathbf{k})\mathbf{v}_v(\mathbf{k})$ distribution along the Fermi surface. Indeed, Figs. 3(e)–3(h) provides a comparison between the LI photocurrents induced by x- and y-polarized light [Figs. 3(e) and 3(g) respectively] and the corresponding quantum metric dipoles [Figs. 3(f) and 3(h)] along the Fermi surface. We observe that the LI photocurrents capture the main features of the quantum metric dipole as a function of azimuthal angle along the Fermi surface.

PD can be used as a "knob" to turn on, control, and amplify quantum geometric photocurrents in a wide range of high symmetry materials even when either $\mathcal{P}$ or $\mathcal{T}$ or both symmetries are intact. Even as we have focused on how PSP enables to probe momentum resolved quantum geometry, from an applied perspective, the selective excitation of carriers enables a novel means of amplifying nonlinear susceptibilities: by exploiting PSP to selectively excite carriers with similar group velocities. As an example, we find PSP enhanced LI susceptibilities as high as $\eta_{yyy}(q) \sim 10^{10} - 10^{11}$ A nmV^{-2}s^{-1} in BLG (a $\mathcal{P}$ and $\mathcal{T}$ preserving material) comparable with those found in 2D ferroelectrics [25].

ACKNOWLEDGMENTS

We gratefully acknowledge useful conversations with Mark Rudner, Qiong Ma, Cheng Liang, Elbert Chia, and Arpit Arora. This work was supported by Singapore MOE Academic Research Fund Tier 3 Grant No. MOE2018-T3-1-002 and a Nanyang Technological University start-up Grant (No. NTU-SUG).

[1] T. Morimoto and N. Nagaosa, Topological nature of nonlinear optical effects in solids, Sci. Adv. **2**, e1501524 (2016).

[2] F. de Juan, A. G. Grushin, T. Morimoto, and J. E. Moore, Quantized circular photogalvanic effect in Weyl semimetals, Nat. Commun. **8**, 15995 (2017).

[3] H. Watanabe and Y. Yanase, Chiral Photocurrent in Parity-Violating Magnet and Enhanced Response in Topological Antiferromagnet, Phys. Rev. X **11**, 011001 (2021).

[4] I. Sodemann and L. Fu, Quantum Nonlinear Hall Effect Induced by Berry Curvature Dipole in Time-Reversal Invariant Materials, Phys. Rev. Lett. **115**, 216806 (2015).

[5] Q. Ma, S.-Y. Xu, H. Shen, D. MacNeill, V. Fatemi, T.-R. Chang, A. M. M. Valdivia, S. Wu, Z. Du, C.-H. Hsu *et al.*, Observation of the nonlinear Hall effect under time-reversal-symmetric conditions, Nature (London) **565**, 337 (2019).

[6] L. Gao, Z. Addison, E. J. Mele, and A. M. Rappe, Intrinsic Fermi-surface contribution to the bulk photovoltaic effect, Phys. Rev. Res. **3**, L042032 (2021).

[7] Q. Ma, A. G. Grushin, and K. S. Burch, Topology and geometry under the nonlinear electromagnetic spotlight, Nat. Mater. **20**, 1601 (2021).

[8] J. Ahn, G.-Y. Guo, and N. Nagaosa, Low-Frequency Divergence and Quantum Geometry of the Bulk Photovoltaic Effect in Topological Semimetals, Phys. Rev. X **10**, 041041 (2020).

[9] Y. Zhang, T. Holder, H. Ishizuka, F. de Juan, N. Nagaosa, C. Felser, and B. Yan, Switchable magnetic bulk photovoltaic effect in the two-dimensional magnet CrI_3, Nat. Commun. **10**, 3783 (2019).

[10] H. Wang and X. Qian, Electrically and magnetically switchable nonlinear photocurrent in PT-symmetric magnetic topological quantum materials, npj Comput. Mater. **6**, 199 (2020).

[11] Y. Kurman, N. Rivera, T. Christensen, S. Tsesses, M. Orenstein, M. Solijačić, J. D. Joannopoulos, and I. Kaminer, Control of semiconductor emitter frequency by increasing polariton momenta, Nat. Photonics **12**, 423 (2018).

[12] A. Woessner, M. B. Lundeberg, Y. Gao, A. Principi, P. Alonso-González, M. Carrega, K. Watanabe, T. Taniguchi, G. Vignale, M. Polini *et al.*, Highly confined low-loss plasmons in graphene–boron nitride heterostructures, Nat. Mater. **14**, 421 (2015).

[13] D. A. Iranzo, S. Nanot, E. J. C. Dias, I. Epstein, C. Peng, D. K. Efetov, M. B. Lundeberg, R. Parret, J. Osmond, J.-Y. Hong *et al.*, Probing the ultimate plasmon confinement limits with a van der Waals heterostructure, Science **360**, 291 (2018).

[14] A. M. Danishevskii, A. A. Kastal'skii, S. M. Ryvkin, and I. D. Yaroshetskii, Dragging of free carriers by photons in direct interband transitions in semiconductors, Sov. Phys. JETP **31**, 292 (1970).

[15] A. F. Gibson, M. F. Kimmitt, and A. C. Walker, Photon Drag in Germanium, Appl. Phys. Lett. **17**, 75 (1970).

[16] M. V. Entin, L. I. Magarill, and D. L. Shepelyansky, Theory of resonant photon drag in monolayer graphene, Phys. Rev. B **81**, 165441 (2010).

[17] J. Maysonnave, S. Huppert, F. Wang, S. Maero, C. Berger, W. de Heer, T. B. Norris, L. A. De Vaulchier, S. Dhillon, J. Tignon *et al.*, Terahertz generation by dynamical photon drag effect in graphene excited by femtosecond optical pulses, Nano Lett. **14**, 5797 (2014).

[18] V. A. Shalygin, M. D. Moldavskaya, S. N. Danilov, I. I. Farbshtein, and L. E. Golub, Circular photon drag effect in bulk tellurium, Phys. Rev. B **93**, 045207 (2016).

[19] E. L. Ivchenko, *Optical Spectroscopy of Semiconductor Nanostructures* (Alpha Science, Harrow, UK, 2005).

[20] S. D. Ganichev and W. Prettl, *Intense Terahertz excitation of semiconductors* (Oxford University Press, Oxford, 2006).

[21] M. M. Glazov and S. D. Ganichev, High frequency electric field induced nonlinear effects in graphene, Phys. Rep. **535**, 101 (2014).

[22] H. Plank, L. E. Golub, S. Bauer, V. V. Bel'kov, T. Herrmann, P. Olbrich, M. Eschbach, L. Plucinski, C. M. Schneider, J. Kampmeier *et al.*, Photon drag effect in $(Bi_{1-x}Sb_x)_2Te_3$ three-dimensional topological insulators, Phys. Rev. B **93**, 125434 (2016).

[23] N. Rivera, I. Kaminer, B. Zhen, J. D. Joannopoulos, and M. Soljačić, Shrinking light to allow forbidden transitions on the atomic scale, Science **353**, 263 (2016).

[24] F. H. L. Koppens, D. E. Chang, and F. J. G. de Abajo, Graphene plasmonics: A platform for strong light matter interactions, Nano Lett. **11**, 3370 (2011).

[25] H. Wang and X. Qian, Ferroicity-driven nonlinear photocurrent switching in time-reversal invariant ferroic materials, Sci. Adv. **5**, eaav9743 (2019).

[26] V. Silkin and D. Svintsov, Plasmonic drag photocurrent in graphene at extreme nonlocality, Phys. Rev. B **104**, 155438 (2021).

[27] R. von Baltz and W. Kraut, Theory ofthe bulk photovoltaic effect in pure crystals, Phys. Rev. B **23**, 5590 (1981).

[28] J. E. Sipe and A. I. Shkrebtii, Second-order optical response in semiconductors, Phys. Rev. B **61**, 5337 (2000).

[29] L.-k. Shi, D. Zhang, K. Chang, and J. C. W. Song, Geometric Photon-Drag Effect and Nonlinear Shift Current in Centrosymmetric Crystals, Phys. Rev. Lett. **126**, 197402 (2021).

[30] L.-k. Shi and J. C. W. Song, Shift vector as the geometric origin of beam shifts, Phys. Rev. B **100**, 201405(R) (2019).

[31] See Supplemental Material at http://link.aps.org/supplemental/10.1103/PhysRevB.106.205423 for a discussion on the quantum geometric interpretation of PD shift and injection photocurrents, symmetry analysis, enhanced nonlinearity by PSP, and c, v band symmetry in bilayer graphene.

[32] D. Rees, K. Manna, B. Lu, T. Morimoto, H. Borrmann, C. Felser, J. E. Moore, D. H. Torchinsky, and J. Orenstein, Helicity-dependent photocurrents in the chiral Weyl semimetal RhSi, Sci. Adv. **6**, eaba0509 (2020).

[33] T. Holder, D. Kaplan, and B. Yan, Consequences of time-reversal-symmetry breaking in the light-matter interaction: Berry curvature, quantum metric, and diabatic motion, Phys. Rev. Res. **2**, 033100 (2020).

[34] F. de Juan, Y. Zhang, T. Morimoto, Y. Sun, J. E. Moore, and A. G. Grushin, Difference frequency generation in topological semimetals, Phys. Rev. Res. **2**, 012017(R) (2020).

[35] O. Matsyshyn, F. Piazza, R. Moessner, and I. Sodemann, Rabi Regime of Current Rectification in Solids, Phys. Rev. Lett. **127**, 126604 (2021).

[36] E. McCann and M. Koshino, The electronic properties of bilayer graphene, Rep. Prog. Phys. **76**, 056503 (2013).